The DOI for this manuscript is doi: 10.1175/JPO-D-16-0266.1

Frontal circulation and submesoscale variability during the formation of a Southern Ocean mesoscale eddy

Katherine A. Adams* and Philip Hosegood

School of Marine Science and Engineering, Plymouth University

John R. Taylor

Department of Applied Mathematics and Theoretical Physics, University of Cambridge

Jean-Baptiste Sallée

Sorbonne Universités, UPMC/CNRS, LOCEAN Laboratory

Scott Bachman

Department of Applied Mathematics and Theoretical Physics, University of Cambridge

Ricardo Torres

Plymouth Marine Laboratory

Megan Stamper

Department of Applied Mathematics and Theoretical Physics, University of Cambridge

**Corresponding author address:* School of Marine Science and Engineering, Plymouth University, Drake Circus, Plymouth, United Kingdom.

17 E-mail: kate.adams@plymouth.ac.uk

ABSTRACT

Observations made in the Scotia Sea during the May 2015 Surface Mixed Layer Evolution at Submesoscales (SMILES) research cruise captured submesoscale, O(1-10 km), variability along the periphery of a mesoscale O(10-100 km) meander precisely as it separated from the Antarctic Circumpolar Current (ACC) and formed a cyclonic eddy $\sim$ 120 km in diameter. The meander developed in the Scotia Sea, an eddy-rich region east of the Drake Passage where the Subantarctic and Polar fronts converge and modifications of Subantarctic mode water (SAMW) occur. *In situ* measurements reveal a rich submesoscale structure of temperature and salinity and a loss of frontal integrity along the newly-formed southern sector of the eddy. A mathematical framework is developed to estimate vertical velocity from co-located drifter and horizontal water velocity time series, under certain simplifying assumptions appropriate for the current data set. Upwelling (downwelling) rates of O(100 m day $^{-1}$) are found in the northern (southern) eddy sector. Favorable conditions for submesoscale instabilities are found in the mixed layer, particularly at the beginning of the survey in the vicinity of density fronts. Shallower mixed layer depths and increased stratification are observed later in the survey on the inner edge of the front. Evolution in T-S space indicates modification of water mass properties in the upper 200 m over 2 days. Modifications along σ_θ 27 - 27.2 kg m^{-3} have climate-related implications for mode and intermediate water transformation in the Scotia Sea on finer spatiotemporal scales than observed previously.

1. Introduction

The Southern Ocean hosts the most energetic current system in the world, the Antarctic Circumpolar Current (ACC). Zonally unbounded by land, the ACC connects ocean basins and transports an estimated 173 Sv through the Drake Passage (Donohue et al. 2016). The ACC is predominantly in geostrophic balance with sea surface height (SSH) gradients and lateral density gradients, hereafter fronts. Large-scale instabilities in the balanced ACC flow cause mesoscale, O(10-100 km), meanders and eddies in the Southern Ocean. While the rich mesoscale structure of the ACC has been studied intensely, finer-scale variability along Southern Ocean fronts is less understood and observed.

Two of the most prominent fronts in the Southern Ocean are the Subantarctic and Polar fronts (hereafter, SAF and PF). Due to sparse data coverage in the Southern Ocean, altimetry-based frontal definitions have been developed; SSH_{SAF} = -0.25 m and SSH_{PF} = -0.70 m are updated values from Sallée et al. (2008). North of the SAF, water masses such as Subantarctic Mode water (SAMW) and Antarctic Intermediate water (AAIW), subduct along isopycnals at specific locations in the Southern Ocean, such as the Scotia Sea (Sallée et al. 2010). The subducted pools of SAMW and AAIW observed north of the ACC contain high levels of anthropogenic CO_2 (Sabine et al. 2004; Pardo et al. 2014) and heat (Frölicher et al. 2015). Currently, SAMW is thought to be transformed by air-sea buoyancy fluxes (Cerovecki et al. 2013) and subsequently mixed and subducted with AAIW, $\sigma_{\theta 27.2}$, to the South Atlantic (Sallée et al. 2010). In locations 'upstream' of the subducted SAMW/AAIW pools, mode water transformation occurs in the mixed layer at the SAF and has climatic implications. The large-scale, O(100-1000 km), physical processes, such as wind-driven and eddy-driven Ekman pumping, responsible for the subduction of heat and carbon in SAMW/AAIW pools have been discussed and documented, e.g. Sallée et al. (2010, 2012), but

very little is known about subduction associated with smaller scales processes (Naveira Garabato et al. 2001).

A potentially important class of dynamics responsible for modulating the vertical exchange at fronts in the Southern Ocean occurs at the submesoscale, O(1-10 km). The oceanic submesoscale is instrumental in extracting energy from density fronts and transferring the energy from mesoscale to submesoscale and dissipative scales (Thomas and Taylor 2010; Capet et al. 2008). The downscale transfer of energy results in ageostrophic motions with large vertical velocities, O(100 m day^{-1}) (Mahadevan and Tandon 2006; Capet et al. 2008; Thomas et al. 2008) capable of transporting heat and tracers across the base of the mixed layer. Where energetic submesoscale processes exist, the resulting vertical buoyancy fluxes may attain an importance equal to or greater than those forced by air-sea exchange.

The presence of fronts preconditions the mixed layer to the development of submesoscale processes, which are characterized by O(1) Rossby (Ro) and balanced Richardson (Ri_B) numbers (Thomas et al. 2008). Submesoscale dynamics are often associated with hydrodynamic instabilities including baroclinic mixed layer instability (MLI), symmetric instability (SI), inertial instability (II) and gravitational instability (GI) (Haine and Marshall 1998; Fox-Kemper et al. 2008; Thomas et al. 2008). These instabilities, with the exception of GI, grow at the expense of available potential energy associated with lateral density gradients (MLI) or thermal wind kinetic energy (II and SI). In each of these cases, instabilities are likely to develop at fronts and can significantly modify the mixed layer density structure (Boccaletti et al. 2007; Hosegood et al. 2008; Taylor and Ferrari 2009; Mahadevan et al. 2010). GI, conversely, is convectively-driven and generated by unstable vertical stratification. Mixing associated with GI leads to deeper mixed layers, while MLI and SI results in restratification.

Sampling submesoscale processes presents challenges due to the complex dynamics of the mixed layer and the short spatiotemporal scales of variability, from hours to days and meters to kilometers. Very few submesoscale-resolving measurements have been made in the Southern Ocean (Rocha et al. 2016), though a recent modeling study has demonstrated the dependence of submesoscale vertical velocities on an energetic mesoscale eddy and strain field (Rosso et al. 2015). An energetic submesoscale is, therefore, expected in a region with high mesoscale EKE, such as the Scotia Sea, a mesoscale eddy hot spot (Frenger et al. 2015). Large, high-*Ro* meanders of the SAF and PF fronts (Figure 2) are indicative of a highly energetic mesoscale field in the Scotia Sea region, suggesting the presence of a similarly energetic submesoscale field.

Here we present novel observations of submesoscale variability in the Southern Ocean from the SMILES (Surface Mixed Layer Evolution at Submesoscales) project, `http://www.smiles-project.org`. SMILES aims to (1) characterize submesoscale dynamics and (2) evaluate the role of submesoscales in mode water transformation in the Scotia Sea using a combination of observations and models. The observational component of the SMILES project consists of a single research cruise to the Scotia Sea in May 2015, just before the austral winter. During a drifter-following cross-front survey, a northward meander of the SAF and PF (Figure 2) separated from the ACC and formed a cold-core mesoscale eddy.

In this paper, we focus on the observed frontal circulation and submesoscale variability along the periphery of the newly-formed eddy. Data sources and processing methods are described in Section 2. Results from the drifter-following survey are presented as follows in Section 3: a) eddy formation, b) frontal circulation, c) cross-frontal variability, and d) water mass modification. Section 4 presents an estimation of vertical velocity and a submesoscale instability analysis with implications for mode water modification. In Section 5, results are summarized and the implications of submesoscale processes during eddy formation in the Scotia Sea are discussed.

2. Data Sources and Methods

Ship-based data sources

The field component of the SMILES project consisted of a Scotia Sea research cruise, 22 April - 21 May 2015, performed aboard the British Antarctic Survey RRS James Clark Ross (JCR). Seasoar, a winged and towed body equipped with a Seabird-Electronics Inc. SBE911, collected temperature, conductivity, and pressure measurements at 16 Hz. Seasoar data is collected in a saw-tooth pattern (Figure 3) at 8 knots ($\sim$ 4 m s^{-1}) with a horizontal spacing between apogees of 2 km for 200-m dives. Temperature and salinity variables were binned to 0.5 dbar intervals. Binned data were gridded using a 2-dimensional Gaussian interpolation scheme (Barnes 1964) with regular spacing, 0.5-km horizontal and 1-m vertical, and decorrelation radii of 1 km and 2 m (Figure 3c).

Horizontal currents were collected in 8-m depth bins over 22 to 600 m of the water column by the ship-mounted RDI Ocean Sciences 75-kHz acoustic doppler current profiler (ADCP). The collected data was cleaned, corrected for ship speed and heading, and ensemble averaged to 150-second bins using Common Ocean Data Access System (CODAS) processing tools. North and east velocity components from 30 - 200 m were gridded to the same grid as the Seasoar data then rotated into along-front and cross-front velocity components using the drifter trajectories as explained below. Error velocities reported from the ADCP processing software are used as estimates of velocity uncertainty in the calculations in Section 4a.

Drogued drifters

A triplet of drogued drifters was used in the survey to estimate horizontal water velocities at 50-m depth. The drifters consisted of a sealed buoy with GPS and satellite communications, a 'holey-

sock' drogue 10-m long and 90-cm in diameter centered at 50-m depth, and 3.5 mm Dyneema line. This design provided a drag area ratio of 44 which is accurate to follow water parcels to within 1 cm s^{-1} (Sybrandy et al. 2009). Drifter location updates were received at 10-minute intervals.

The drifters were released in the northern portion of the meander just south of the maximum jet velocity and temperature gradient (Figure 3a) for the first Seasoar leg of the survey. In a current of $\sim$1.25 m s^{-1}, the three minute separation of the drifter releases yields an initial along-front drifter separation of $\sim$225 m. The trajectory of the first drifter released, D16, was chosen to define the along-front direction in the survey analysis, θ_{along} (Table 1). The along-front reference frame assumes the drifter maintains its position in the front and jet, which is shown in Figure 4. The closest drifter crossing in time and space of each Seasoar leg defines the center of each section, with cross-frontal distance increasing outward, or away, from the eddy center. Each leg was rotated to a cross-front heading, θ_{cross}, defined as the orthogonal direction to θ_{along} for each respective Seasoar leg (Table 1). Similarly, measured horizontal water velocities were rotated into along-front and cross-front components for each leg.

Remote data sources

Satellite sea surface temperature (SST) and sea surface height (SSH) data were used for mesoscale frontal and eddy detection during the cruise and the analysis. Both data sets are available daily on a 0.25° grid. Figure 2 is an example of the remote sensing data available during the SMILES cruise. The daily, gridded optimally interpolated microwave SST data (OISST) was obtained from Remote Sensing Systems, (`http://www.remss.com`). SSH, or absolute dynamic topography, and altimetrically-derived geostrophic surface current data were downloaded from AVISO Cnes (`www.aviso.altimetry.fr`) (Pujol et al. 2016). SAF and PF positions are defined

using SSH contours of -0.25 m and -0.7 m, respectively, updated from the definitions in Sallée et al. (2008).

3. Results

a. Eddy formation

A northward meander of the Subantarctic front (SAF) and Polar front (PF) developed along the Antarctic Circumpolar Current (ACC) (Figure 2) in late April 2015. This mesoscale, $O(100$ km), feature characterized by meridional changes of 4°C SST and 0.5-m SSH over 50 km, formed just south of the North Scotia Ridge. Antarctic surface water, <2°C south of the PF (Orsi et al. 1995), is observed in the center of the meander. The vorticity Rossby number, $Ro = \zeta f^{-1}$, of the meander as calculated from altimetry-derived geostrophic surface currents from 20 April is ~ 0.4. This moderate *Ro* value based on coarse altimetry data does not account for ageostrophic contributions from curvature of the flow, e.g. cyclogeostrophic flow. Although the moderate *Ro* estimate is high compared to previous submesoscale-focused process studies, e.g. $Ro \sim 0.1$ in the North Pacific (Hosegood et al. 2013), it not uncommon for this region.

A triplet of drogued drifters released in the northwest sector of the meander on 08 May 2015 20:00 GMT was followed with the RRS JCR while towing the Seasoar CTD perpendicular to the drifter trajectories. The daily progression of SST, SSH, drifter trajectories and the ship track are presented in Figure 4 for 8-12 May 2015. At the time of the drifter release, 18 days after the SST and SSH observations presented in Figure 2, the meander had sharpened yet remained tethered to the ACC as observed by SST and SSH fields, Figure 4a. During the survey, the drifters initially traveled east (Figure 4b) and southeast (Figure 4c) around the meander and remarkably continued along a cyclonic trajectory precisely as the meander separated from the ACC and formed

a cold closed-core eddy, Figure 4c-e. Initially, the cyclonic eddy measured approximately 120-km in diameter with a dynamic height anomaly of 0.5 m (-0.2 to -0.7 m SSH). After the eddy formed, Figure 4e, the SAF and PF returned to a zonal orientation south of the eddy. Hereafter, the meander/eddy feature will be referred to as an eddy for the duration of the Seasoar survey.

The Seasoar survey, shown as the ship track in Figure 4, consisted of 25 sections around the edge of the eddy ranging from 25 - 40 km in length. Maps of 10-m depth temperature and salinity from these 25 sections are presented in Figure 5a-b. The beginning northern sector of the survey is characterized by sharp temperature and salinity fronts (2°C, 0.2 psu in 2 km at 4-m depth) with warm, salty water outside and cold, fresh waters inside the eddy. A region characterized by a loss of temperature and salinity frontal integrity is observed along the southern portion of the survey. The repeat observation of temperature and salinity intrusions in consecutive sections suggests the presence of a 3-dimensional structure such as a submesoscale streamer or filament, only a few kilometers across, in the newly-formed southern eddy sector. Note that the filaments occur in a region that was previously an open meander characterized by weak lateral gradients in temperature and salinity.

Horizontal water velocities measured at 50-m depth are included in Figure 5c-d where the along-front and cross-front components are determined relative to a drifter trajectory direction (Table 1) for each Seasoar section. A $\sim$ 70% decrease (1.5 to 0.4 m s^{-1}) in drifter and along-front water velocities is observed from the N to S legs. Geostrophic surface velocity vectors (Figure 4) also show weaker currents in the southern portion of the eddy compared to the north. A sign change in cross-frontal velocities on either side of the drifters indicates diffluent flow during the majority of the survey with confluent cross-frontal flow in the southern portion of the survey.

The ageostrophic component of the curved flow around the eddy can be estimated from the along-frontal velocities by comparing the centripetal acceleration term with the Coriolis acceler-

ation, $C = u(Rf)^{-1}$. Assuming an eddy radius, $R = 50$ km, C is maximum along the northern portion of the survey (0.25) and minimum (0.10) in the southern eddy sector. This indicates a larger cyclogeostrophic component to the flow in the north.

Wind forcing during the Seasoar survey was unusually calm for April in the Southern Ocean with wind speeds < 10 m s^{-1} and winds from SE to NW rather than the expected westerlies.

A partial infrared SST image of the eddy was captured during the Seasoar survey by an AVHRR sensor aboard the Metop-a satellite on 11 May 2015 at 12:42 GMT (Figure 6a). The high-resolution (1 km) SST data show strong gradients along the northern eddy boundary and weaker gradients to the southeast, similar to Figure 5a. Unfortunately, clouds mask the southern and western sectors of the eddy. The ship's underway temperature data at 4-m depth is overlaid on the infrared SST data in Figure 6b. The noticeable offset in temperatures is due to the northward movement of the eddy in the 2.5 days between the beginning of the survey and the satellite measurements. The ship's temperature data is also plotted atop optimally-interpolated microwave SST data for 11 May 2015. The eddy boundary, defined by the 3°C isotherm in Figure 6a and c is drastically different between the 1-km infrared and coarser microwave SST data.

b. Cross-frontal variability

Vertical cross-sections of potential density anomaly (σ_θ, kg m^{-3}), temperature (°C), salinity, and horizontal water velocities (m s^{-1}) are presented in Figure 7 for the Seasoar legs labeled in Figure 5. The five sections span approximately two days and 180 degrees of heading of the drifter-following survey. Each section is referenced in a similar manner with respect to the front; the left (right) -hand side of the sections will be referred to as inner (outer) with negative (positive) cross-frontal distance. Since the sections are centered using the drifter trajectories, a cross-frontal distance of zero is not an explicit definition of the frontal center with respect to density.

In Leg N, σ_θ increases laterally away from the eddy core except for a dense filament $\sim$ 5 km in width located in the center of the leg (Figure 7a). The filament, with temperatures < 1.5°C, is observed between two outcropping isopycnals with a potential density anomaly of 27.0 kg m^{-3} (hereafter $\sigma_{\theta 27}$). The inner density gradient, 0.09 kg m^{-3} in 5 km, is nearly twice the magnitude of the warm, outer density front, 0.04 kg m^{-3} in 5 km. In Leg E, the $\sigma_{\theta 27}$ is observed subsurface. By Leg S, the depth of the $\sigma_{\theta 27}$ is much shallower on the inner side of the leg.

Mixed layer depth, MLD, defined as the level of a 0.01 kg m^{-3} density increase from 5-m depth, is included in Figure 7a. This strict MLD definition was chosen to highlight the lateral density gradients in the current dataset. Values of MLD are O(100 m) for most of Leg N. In each leg, the mixed layer is shallowest within the density fronts, <50 m, and deepest within the dense filament at 130 m. The MLD shoals similarly to $\sigma_{\theta 27}$ in Leg S, suggestive of restratification of the inner front along the newly-formed sector of the eddy. The shallower MLD may be the result of temporal variability, e.g., restratification from submesoscale instabilities, or spatial variability.

Temperature and salinity fields vary similarly across the sections, Figure 7b-c, due to strong density compensation, characteristic of ACC fronts. In Leg N, the warm, salty outer region lies adjacent to a cold, dense filament at a cross-front distance of 0 km. Leg E, in the east sector of the survey, contains a small subsurface cold water intrusion at 120-m depth and 10-km cross-front distance. Intrusions of cold, fresh water on the outer side and warm, salty water on the inner side are observed in all legs collected in the east and southeast sectors of the survey. In leg SE, the intrusion is larger in vertical and horizontal extent and outcropped. In Leg S a loss of frontal integrity is observed compared to the well-organized, separated cold-fresh inner and warm-salty outer regions present in Leg N.

Vertical cross-sections of along-front and cross-front velocities, Figure 7d-e, show a strong barotropic component to the flow. Trends throughout the survey agree with the 50-m maps in

Figure 5c-d. Along-front velocities decrease whereas cross-front velocities switch from confluent to diffluent from Legs N to S.

c. Frontal circulation

The frontal circulation at the center of each Seasoar leg can be described using the co-located drifter and horizontal water velocity datasets. As shown in Figure 8a, the drifter and along-front water velocities at 50-m depth are in strong agreement. Drifters initially deployed in the northern sector of the cyclonic eddy decelerated around the eastern side toward the southern sector where the along-front velocity is minimum, after which the drifters accelerated around the western edge. Similar trends were observed in the measured along-front velocity. The cross-frontal gradient of cross-frontal velocity, was positive (diffluent) during the along-front deceleration and negative (confluent) during the along-front acceleration as shown in (Figure 8b).

4. Analysis

a. Estimation of vertical velocity

Vertical velocities, w, were not directly measured in the SMILES Seasoar survey. However, the co-located drifter and ADCP datasets allow for the following mathematical framework which yields a solvable expression for w at a specific depth and a cross-frontal location in each Seasoar leg. Assumptions made in the following derivation are tested in Appendix A.

Let $\mathbf{x}_D(t)$, and $\mathbf{u}_D(t)$ be the measured drifter position and velocity vectors at time t where

$$\left(\frac{dx_D}{dt}, \frac{dy_D}{dt}\right) = \Big(u_D(t), v_D(t)\Big). \tag{1}$$

Let $\mathbf{u}_E(x,y,z,t)$ be the Eulerian fluid velocity. Assume that the drifter moves with the vertically averaged Eulerian velocity at the horizontal location of the drogue from depth z_1 to z_2

$$\frac{d\mathbf{u}_D}{dt} = \frac{d}{dt}\left[\bar{\mathbf{u}}_E(x_D(t), y_D(t), t)\right] \tag{2}$$

where

$$\bar{\mathbf{u}}_E \equiv \frac{1}{z_1 - z_2}\int_{z_2}^{z_1} \mathbf{u}_E\, dz. \tag{3}$$

Here we set $z_1 = 0$ at the surface and $z_2 = 50$ m, the drifter drogue depth. This assumes the drogued drifter is moving with the depth-integrated Eulerian velocity in the top 50-m of the water column. Justification for this assumption is presented in the Appendix. Expanding the derivative in (2),

$$\frac{d\mathbf{u}_D}{dt} = \frac{\partial \bar{\mathbf{u}}_E}{\partial t} + \frac{dx_D}{dt}\frac{\partial \bar{\mathbf{u}}_E}{\partial x} + \frac{dy_D}{dt}\frac{\partial \bar{\mathbf{u}}_E}{\partial y} = \frac{\partial \bar{\mathbf{u}}_E}{\partial t} + \bar{\mathbf{u}}_E \cdot \nabla_H \bar{\mathbf{u}}_E. \tag{4}$$

where $\nabla_H \equiv (\frac{\partial}{\partial x}, \frac{\partial}{\partial y})$. From continuity, $\nabla \cdot \mathbf{u}_E \equiv 0$ hence $\nabla \cdot \bar{\mathbf{u}}_E = 0$ for constant z_1 and z_2,

$$\frac{\partial \bar{u}_E}{\partial x} + \frac{\partial \bar{v}_E}{\partial y} + \frac{w_E(x_D, y_D, z_1, t) - w_E(x_D, y_D, z_2, t)}{z_1 - z_2} = 0. \tag{5}$$

From (4), the rate of change of the along-front drifter velocity is

$$\frac{du_D}{dt} = \frac{\partial \bar{u}_E}{\partial t} + \bar{u}_E\frac{\partial \bar{u}_E}{\partial x} + \bar{v}_E\frac{\partial \bar{u}_E}{\partial y} \tag{6}$$

while (5) gives

$$\frac{\partial \bar{u}_E}{\partial x} = -\frac{\partial \bar{v}_E}{\partial y} - \frac{w_E|_{z_1} - w_E|_{z_2}}{z_1 - z_2}. \tag{7}$$

Substituting (7) in (6) gives

$$\frac{du_D}{dt} = \frac{\partial \bar{u}_E}{\partial t} - \bar{u}_E\frac{\partial \bar{v}_E}{\partial y} - \bar{u}_E\frac{w_E|_{z_1} - w_E|_{z_2}}{z_1 - z_2} + \bar{v}_E\frac{\partial \bar{u}_E}{\partial y}. \tag{8}$$

Re-arranging (8) yields an expression for the difference of vertical velocity from z_1 to z_2

$$w_E|_{z_1} - w_E|_{z_2} = (z_1 - z_2)\left[-\frac{1}{\bar{u}_E}\frac{du_D}{dt} + \frac{1}{\bar{u}_E}\frac{\partial \bar{u}_E}{\partial t} - \frac{\partial \bar{v}_E}{\partial y} + \frac{\bar{v}_E}{\bar{u}_E}\frac{\partial \bar{u}_E}{\partial y}\right]. \tag{9}$$

An expression for w_E at the drogue depth, z_2, is obtained by setting $w_E(z_1 = 0) = 0$,

$$w_E|_{z_2} = z_2 \left[\frac{1}{\bar{u}_E} \frac{du_D}{dt} - \frac{1}{\bar{u}_E} \frac{\partial \bar{u}_E}{\partial t} + \frac{\partial \bar{v}_E}{\partial y} - \frac{\bar{v}_E}{\bar{u}_E} \frac{\partial \bar{u}_E}{\partial y} \right]. \tag{10}$$

We can make a steady-state assumption,

$$\frac{\partial \bar{u}_E}{\partial t} \ll \frac{du_D}{dt}, \tag{11}$$

if local accelerations are smaller than drifter accelerations on time scales greater than a day, the filtering window of the drifter velocities. This is tested in the Appendix making use of ship track intersections during the survey. We then have an expression,

$$w_E|_{z_2} = z_2 \left[\frac{1}{\bar{u}_E} \frac{du_D}{dt} + \frac{\partial \bar{v}_E}{\partial y} - \frac{\bar{v}_E}{\bar{u}_E} \frac{\partial \bar{u}_E}{\partial y} \right], \tag{12}$$

that allows for the calculation of vertical velocity in the center of each Seasoar leg at z_2, the drifter drogue depth of 50 m, (Figure 8d). Velocity components $\bar{u}_E$ and $\bar{v}_E$ are first calculated by averaging velocities from the first good ADCP bin, 30-m, to 50-m, as in Figure 8a. Extrapolations to the surface are used to approximate $\bar{u}_E$ from z = 0 to 50 m, as detailed in the appendix. The cross-frontal velocity gradients, $\frac{\partial \bar{u}_E}{\partial y}$ and $\frac{\partial \bar{v}_E}{\partial y}$, are averaged +/- 1 km from the center of each Seasoar leg (Figure 8b). Error velocities reported by the ADCP processing and propagated through the w calculation are shown as error bars in Figure 8d.

Vertical velocities calculated from (12) are presented in Figure 8d with negative (positive) values during the N-SE (S) eddy survey sectors. Upwelling velocities are calculated during the N, NE and E sectors of the survey, when diffluent cross-front flow and drifter deceleration is observed. Subduction is indicated in the southern survey sector when drifters accelerated. There is a strong dependence on $\frac{\partial \bar{v}_E}{\partial y}$ in our calculation indicating the cross-frontal flow is related to the vertical circulation. The estimated magnitudes of $w_E|_{50m}$, $O(100 \text{ m day}^{-1})$, are similar to reported values for

submesoscale processes, however, we can not discern the relative contributions of the mesoscale and submesoscale vertical motions here.

b. Submesoscale instabilities

Although direct measurements of submesoscale instabilities were not made during the Seasoar survey, it is possible to diagnose whether conditions were favorable for submesoscale instability growth and which specific instabilities were possible (Thomas et al. 2013; Thompson et al. 2016). First, instability development is favored when Ertel potential vorticity (EPV),

$$EPV = \omega_{\mathbf{a}} \cdot \nabla b = (\boldsymbol{f} + \nabla \times \mathbf{u}) \cdot \nabla b, \tag{13}$$

is the opposite sign of f (Hoskins 1974; Haine and Marshall 1998; Thomas et al. 2008); the absolute vorticity, ω_a, is the sum of planetary and relative vorticity and buoyancy is $b = -g\rho'\rho_0^{-1}$. The perturbation density, ρ', is the measured density, ρ, minus the average leg density, ρ_0. This EPV criterion has been shown to hold even in flow regimes where ageostrophic processes such as down-front winds (Thomas and Taylor 2010; Thomas et al. 2013), inertial shear (Thomas et al. 2016) and surface-wave driven shear (Haney et al. 2015) drive symmetric instability.

Expanding (13) gives

$$EPV = (w_y - v_z)b_x + (u_z - w_x)b_y + [f + (v_x - u_y)]b_z, \tag{14}$$

where subscripts indicate a partial derivative and x and y are the along-front and cross-front directions. Neglecting ∂x terms in (14) assumes along-front gradients $\ll$ cross-front gradients. This simplification yields,

$$EPV \simeq (f - u_y)b_z + u_z b_y, \tag{15}$$

an approximation for EPV dependent on cross-front and vertical gradients in the along-front velocity and buoyancy. The 2-dimensional approximation of EPV (15) is shown in Figure 9 below the

cross-frontal buoyancy gradient at 10-m depth which identifies density fronts in each leg. Regions with positive EPV ($f < 0$) are favorable for the instabilities described above and are observed on either side of the lateral buoyancy gradients, or fronts, and mostly above the MLD. The band of negative EPV in each leg is stable to instabilities due to the strong vertical stratification, b_z, of the ML base.

The EPV calculation in (15), expressed in the local Cartesian coordinate system for each Seasoar leg, neglects effects due to the curved flow around the eddy. We now consider EPV in cylindrical coordinates (Shakespeare 2016),

$$EPV_{cyl} = (f + u_{\theta_r} + u_\theta R^{-1}) b_z - u_{\theta_z} b_r, \tag{16}$$

where R is the curvature of the flow and the azimuthal velocity, u_θ, is negative in a clockwise (cyclonic) rotational sense. The curvature term, $u_\theta R^{-1} b_z$, is negative in stably stratified conditions ($b_z > 0$) and, therefore will decrease EPV from the estimate in (15). The EPV calculation was repeated using (16) for legs N-S using an eddy radius $R = 50$ km (not shown). The average percent difference in Leg N (Leg S) is 23% (7%), however the inclusion of the curvature term has an indiscernible change on the EPV panels in Figure 9b. The number of locations with EPV $>$ 0 decreased by 0.75% (Leg N) - 0.15% (Leg S). Therefore, the total EPV is slightly lower when curvature effects are considered. This could result in a slight overestimation in the number of locations identified as favorable for inertial and symmetric instabilities below.

For regions where EPV is positive ($f < 0$) specific submesoscale instabilities can be identified using the balanced Richardson number, $Ri_B = f^2 b_z^2 b_y^{-4}$. The criteria presented in Thomas et al. (2013) classifies gravitational ($Ri_B < -1$), mixed gravitational-symmetric ($-1 < Ri_B < 0$), symmetric ($0 < Ri_B < 1$ for $Ro_g < 0$ and $0 < Ri_B < Ro_g^{-1}$ for $Ro_g > 0$), and inertial ($1 < Ri_B < Ro_g^{-1}$ for $Ro_g < 0$) instabilities, as well as stable portions of the water column, $Ri_B > Ro_g^{-1}$. The geostrophic

Rossby number, $Ro_g = \zeta_g f^{-1} \simeq -\frac{\partial u_g}{\partial y} f^{-1}$, is computed using the geostrophic along-front velocity, u_g, rather than the measured (Thompson et al. 2016). Locations favored for specific submesoscale instabilities as diagnosed by Ri_B are presented in Figure 9c.

Throughout the survey, the mixed layer was consistently more susceptible to submesoscale instabilities than the deep, stable regions where EPV$<$0. Gravitational instability is most likely early in the survey and away from density fronts where MLD are large. The criteria for mixed and symmetric instabilities are met within density fronts in Legs N - E. Conditions conducive for inertial, or centrifugal, instability are located on the outer (right-hand) side with $Ro_g = \zeta_g f^{-1} < 0$.

Regions where conditions are conducive to the development of submesoscale instabilities are shown as a fraction of the mixed layer in Figure 9d. There is a general decrease between the N and S legs, indicating a greater proportion of the ML is more prone to instabilities earlier in the survey versus in the legs collected in the southern sector of the eddy. Throughout the survey, the majority of the instability indications are for gravitational with conditions favorable for symmetric or mixed gravitational and symmetric concentrated near lateral density gradients.

c. Water mass modification

The sharp temperature and salinity fronts across the eddy boundary indicate the presence of different water masses. T-S histograms for Seasoar sections N-S, Figure 10a, show the prevalence of measurements in 0.15°C and 0.015 salinity bins. In Leg N the T-S measurements largely populate two separate regions in T-S space, with cold, fresh inner waters in the bottom left of the diagram and the warm, salty (spicy) outer region measurements in the top right. The two regions in T-S space are connected via $\sigma_{\theta 27}$, the isopycnal that outcrops on either side of the dense filament at the front center in Leg N, previously presented in Figure 7. A similar connection along deeper isopy-

cnals, such as $\sigma_{\theta 27.2}$, is not observed in Leg N (Figure 10). This is due to an unequal isopycnal upheaval across the Seasoar leg and the 200-m depth limit of the dataset.

A cross-front exchange is observed in Legs NE-E as cool, fresh measurements $\sigma_{\theta 27 \text{ - } 27.2}$ extend into warmer and saltier T-S space. By Leg S, the T-S space is fully populated indicating mixing or advection of new water masses, not previously observed at the start of the survey. Locations previously identified as susceptible to submesoscale instabilities in Section 4b are shown in T-S space (Figure 10b). Instabilities are mostly favored along the $\sigma_{\theta 27}$, supporting an along isopycnal exchange across the frontal region. The exchange or modification along $\sigma_{\theta 27.1 \text{ - } 27.2}$ suggests that water mass properties below the MLD are also affected on timescales of O(1 day) and horizontal length scales of O(1-10 km) during the formation of this mesoscale eddy.

5. Discussion & Summary

Here we have presented high-resolution observations across the ACC as a cyclonic eddy formed in the Scotia Sea. The novel observations reveal submesoscale frontal variability and two distinct dynamic regimes along the periphery of the eddy as depicted in Figure 11.

In the northern to eastern regime of the survey, diffluent flow and deceleration were observed in the cross-front and along-front directions, respectively. Along the newly-formed southern edge of the eddy, along-front acceleration and cross-front confluent flow is observed coincident with a complex T-S structure, similar to submesoscale features found in other studies, e.g. filaments and streamers (Gula et al. 2014; Klymak et al. 2016). A submesoscale instability analysis identified regions across each cross-frontal section prone to the development of gravitational, mixed, symmetric and inertial instabilities. Favorable conditions for mixed and symmetric instabilities were found near large cross-frontal density gradients in the mixed layer throughout the survey. Despite the loss of frontal integrity observed in the southern regime, the eddy discussed here maintained a

distinct signature in SST and SSH over the following two months as evidenced by remote sensing imagery.

The Scotia Sea hosts an especially high abundance of mesoscale eddies (Frenger et al. 2015) in the eddy-rich Southern Ocean. Eddy kinetic energy (EKE) in this region, calculated from time-mean removed, altimetry-derived geostrophic surface currents (AVISO; 1993-2015) is O(0.1 - 1 $m^2\ s^{-2}$). Recent submesoscale-resolving modeling results indicate a strong correlation between mesoscale EKE and submesoscale vertical velocity in the Southern Ocean (Rosso et al. 2015) implicating a downscale energy transfer. Although the Scotia Sea EKE values and w esimates presented here are much higher than the domain-averaged magnitudes reported in Rosso et al. (2015), the trend of high EKE and high w is consistent.

The strong vertical circulation found at the SAF, suggests that submesoscale processes might be critical in transforming and subducting mode and intermediate waters, although such processes have been mostly ignored in previous studies. Water mass properties across the frontal region were initially observed as a cold, fresh eddy region and a warm, salty outer region. The rapid spread in T-S space suggests mixing occurred during the eddy formation. Enhanced vertical circulation and mixing, prompted by submesoscale processes, have the potential to transform mode and intermediate water density classes and contribute to the uptake of anthropogenic heat and carbon to the Southern Ocean. A quantification of the net water-mass subduction associated with the observed circulation will be part of a future study.

Cyclonic mesoscale eddies have been observed with high chlorophyll signatures in the Scotia Sea (Kahru et al. 2007), implicating their importance on primary production in the region. Studies resolving submesoscale dynamics in mesoscale eddies have shown that strong vertical velocities, like those presented here, may drive the vertical exchange in the upper ocean with important effects on nutrient supply to the photic zone (Lévy et al. 2001; Mahadevan et al. 2008; Lévy et al. 2012;

Mahadevan 2016). The biogeochemical responses within the eddy observed during the SMILES cruise are a focus of a future study.

Acknowledgments. The SMILES project is funded through the National Environmental Research Council, standard grant NE/J009857/1. JR311 data collection and technical support were received from the British Antarctic Survey, the crew of RRS James Clark Ross, and the NEODAAS and PML remote sensing groups. Seasoar operations were led by National Marine Facilities technicians Paul Provost, Dougal Mountifield, Julie Wood, and Candice Cameron, from the UK National Oceanographic Centre. Peter Ganderton designed and built the drifter electronics package. The altimeter products were produced by Ssalto/Duacs and distributed by Aviso, with support from Cnes (http://www.aviso.altimetry.fr/duacs/). Microwave OI SST data are produced by Remote Sensing Systems and sponsored by National Oceanographic Partnership Program (NOPP) and the NASA Earth Science Physical Oceanography Program.

APPENDIX

The derivation of the vertical velocity presented in Section 4a requires two key assumptions. The first relates to the depth range over with the drifter acceleration is valid, and the second requires that the local Eulerian acceleration is much smaller than the drifter acceleration. Both assumptions have critical implications for the estimate of vertical velocity and we thus expand on the justification for making these assumptions below.

Assumption in (2): $\frac{d\mathbf{u}_D}{dt} = \frac{d}{dt}\left[\bar{\mathbf{u}}_E(x_D(t), y_D(t), t)\right]$

The assumption presented in (2) sets the drifter acceleration equal to the depth-averaged Eulerian acceleration from the drogue depth of 50 m to the surface. If the drifter has a sufficient drag ratio (see Section 2), this assumption is justified and $u_D \sim \bar{u}_E$. A comparison of u_D and

the $\bar{u}_E$ from 30 - 50 m, presented in Figure A1a, shows very strong agreement. Due to the blanking distance of the 75 kHz ADCP, measurements of u_E are only available for depths below 30 m. Slab and linear extrapolations from 30 m to the surface are used to approximate $\bar{u}_E$ from 0 to 50 m. The depth-integrated 30-50 m Eulerian velocities and depth-integrated extrapolated 0-50 m Eulerian velocities are compared with the drifter velocities in Figure A1b and A1c. The slab-extrapolated approximation is a better fit than the linear extrapolation. The calculation of vertical velocity in Section 4a is carried out with both extrapolation approximations of u_E (Figure 8d).

Assumption in (11): $\frac{\partial \bar{u}_E}{\partial t} \ll \frac{du_D}{dt}$

The steady state assumption in (11) requires the local Eulerian acceleration, $\frac{\partial \bar{u}_E}{\partial t}$, in the top 50 m to be much smaller than the drifter acceleration. To check this assumption, we calculate $\frac{\partial \bar{u}_E}{\partial t}$ from ship track intersections during the Seasoar survey, e.g., $\frac{\partial \bar{u}_E}{\partial t} \simeq \frac{u_E(t_2)-u_E(t_1)}{t_2-t_1}$ where t_1 and t_2 are times corresponding to the ADCP measurements for a given ship track intersection. Measurement pairs are matched if separated by less than 250 m horizontally and more than 1 day in time. The time separation criteria is consistent with the filtering window of the drifter velocities. Nine pairs of measurements were found and used to estimate the local Eulerian acceleration, $\frac{\partial \bar{u}_E}{\partial t}$, depth-averaged over 30 to 50 m. Locations of the measurement pairs are shown in Figure A2. The average $\frac{\partial \bar{u}_E}{\partial t}$, -1.3 $\pm$ 1.2 x 10^{-6} (m s^{-2}) is plotted alongside the drifter acceleration time series during the survey. The steady state assumption, (11) in Section 4a, holds for most Seasoar legs where drifter accelerations are larger than the average Eulerian acceleration estimate. In the NE sector of the eddy and a few southern eddy legs, this is not true and the steady state assumption cannot be made from this ship intersection estimate alone.

Additionally, $\frac{\partial \bar{u}_E}{\partial t}$ is estimated from altimeter-derived geostrophic surface currents (not shown). The average values for the survey region are 0.04 ± 0.02 m s^{-1} per day which is an order of magnitude smaller than the average measured drifter accelerations, 0.49 ± 0.29 m s^{-1} per day) and the opposite sign as an expected change in along-front velocity due to the cyclonic eddy rotation.

References

Barnes, S. L., 1964: A Technique for Maximizing Details in Numerical Weather Map Analysis. Journal of Applied Meteorology, 396–409 pp.

Boccaletti, G., R. Ferrari, and B. Fox-Kemper, 2007: Mixed layer instabilities and restratification. *Journal of Physical Oceanography*, **37**, 2228–2250, doi:10.1175/JPO3101.1.

Capet, X., J. C. McWilliams, M. J. Molemaker, and A. F. Shchepetkin, 2008: Mesoscale to Submesoscale Transition in the California Current System. Part I: Flow Structure, Eddy Flux, and Observational Tests. *Journal of Physical Oceanography*, **38 (1)**, 29–43, doi:10.1175/2007JPO3671.1, URL http://journals.ametsoc.org/doi/abs/10.1175/2007JPO3671.1.

Cerovecki, I., L. D. Talley, M. R. Mazloff, and G. Maze, 2013: Subantarctic Mode Water Formation, Destruction, and Export in the Eddy-Permitting Southern Ocean State Estimate. *Journal of Physical Oceanography*, **43 (7)**, 1485–1511, doi:10.1175/JPO-D-12-0121.1, URL http://journals.ametsoc.org/doi/abs/10.1175/JPO-D-12-0121.1.

Donohue, K., D. Watts, P. Hamilton, R. Leben, and M. Kennelly, 2016: Loop Current Eddy Formation and Baroclinic Instability. *Dynamics of Atmospheres and Oceans*, doi:10.1016/j.dynatmoce.2016.01.004, URL http://linkinghub.elsevier.com/retrieve/pii/S0377026516300057.

469 Fox-Kemper, B., R. Ferrari, and R. Hallberg, 2008: Parameterization of Mixed Layer Eddies. Part
470 I: Theory and Diagnosis. *J Phys Oceanogr*, **38 (6)**, 1145–1165, URL http://journals.ametsoc.
471 org/doi/abs/10.1175/2007JPO3792.1.

472 Frenger, I., M. Münnich, N. Gruber, and R. Knutti, 2015: Southern Ocean eddy phenomenology.
473 *Journal of Geophysical Research: Oceans*, **120 (11)**, 7413–7449, doi:10.1002/2015JC011047,
474 URL http://doi.wiley.com/10.1002/2015JC011047.

475 Frölicher, T. L., and Coauthors, 2015: Dominance of the Southern Ocean in Anthropogenic
476 Carbon and Heat Uptake in CMIP5 Models. *Journal of Climate*, **28 (2)**, 862–886, doi:
477 10.1175/JCLI-D-14-00117.1.

478 Gula, J., M. J. Molemaker, and J. C. McWilliams, 2014: Submesoscale cold filaments in the
479 Gulf Stream. *Journal of Physical Oceanography*, **44 (10)**, 140728145042 006, doi:10.1175/
480 JPO-D-14-0029.1, URL http://journals.ametsoc.org/doi/abs/10.1175/JPO-D-14-0029.1.

481 Haine, T. W. N., and J. Marshall, 1998: Gravitational, Symmetric, and Baroclinic Instability of
482 the Ocean Mixed Layer. *Journal of Physical Oceanography*, **28 (4)**, 634–658, doi:10.1175/
483 1520-0485.

484 Haney, S., B. Fox-Kemper, K. Julien, A. Webb, S. Haney, B. Fox-Kemper, K. Julien, and A. Webb,
485 2015: Symmetric and Geostrophic Instabilities in the Wave-Forced Ocean Mixed Layer. *Journal*
486 *of Physical Oceanography*, **45 (12)**, 3033–3056, doi:10.1175/JPO-D-15-0044.1, URL http://
487 journals.ametsoc.org/doi/10.1175/JPO-D-15-0044.1.

488 Hosegood, P. J., M. C. Gregg, and M. H. Alford, 2008: Restratification of the Surface Mixed Layer
489 with Submesoscale Lateral Density Gradients: Diagnosing the Importance of the Horizontal Di-

mension. *Journal of Physical Oceanography*, **38 (11)**, 2438–2460, doi:10.1175/2008JPO3843.1, URL http://journals.ametsoc.org/doi/abs/10.1175/2008JPO3843.1.

Hosegood, P. J., M. C. Gregg, and M. H. Alford, 2013: Wind-driven submesoscale subduction at the north Pacific subtropical front. *Journal of Geophysical Research: Oceans*, **118 (10)**, 5333–5352, doi:10.1002/jgrc.20385, URL http://doi.wiley.com/10.1002/jgrc.20385.

Hoskins, B. J., 1974: The role of potential vorticity in symmetric stability and instability. *Quarterly Journal of the Royal Meteorological Society*, **100 (425)**, 480–482, doi:10.1002/qj.49710042520, URL http://doi.wiley.com/10.1002/qj.49710042520.

Kahru, M., B. G. Mitchell, S. T. Gille, C. D. Hewes, and O. Holm-Hansen, 2007: Eddies enhance biological production in the Weddell-Scotia Confluence of the Southern Ocean. *Geophysical Research Letters*, **34 (14)**, L14 603, doi:10.1029/2007GL030430, URL http://doi.wiley.com/10.1029/2007GL030430.

Klymak, J. M., and Coauthors, 2016: Submesoscale streamers exchange water on the north wall of the Gulf Stream. *Geophysical Research Letters*, **43 (3)**, 1226–1233, doi:10.1002/2015GL067152, URL http://doi.wiley.com/10.1002/2015GL067152.

Lévy, M., R. Ferrari, P. J. S. Franks, A. P. Martin, and P. Rivière, 2012: Bringing physics to life at the submesoscale. *Geophysical Research Letters*, **39 (14)**, n/a–n/a, doi:10.1029/2012GL052756, URL http://doi.wiley.com/10.1029/2012GL052756.

Lévy, M., P. Klein, and A.-M. Treguier, 2001: Impact of sub-mesoscale physics on production and subduction of phytoplankton in an oligotrophic regime. *Journal of Marine Research*, **59 (4)**, 535–565, doi:10.1357/002224001762842181.

Mahadevan, A., 2016: The Impact of Submesoscale Physics on Primary Productivity of Plankton. *Annual review of marine science*, **8**, 161–84, doi:10.1146/annurev-marine-010814-015912, URL http://www.ncbi.nlm.nih.gov/pubmed/26394203.

Mahadevan, A., and A. Tandon, 2006: An analysis of mechanisms for submesoscale vertical motion at ocean fronts. *Ocean Modelling*, **14 (3-4)**, 241–256, doi:10.1016/j.ocemod.2006.05.006, URL http://www.sciencedirect.com/science/article/pii/S1463500306000540.

Mahadevan, A., A. Tandon, and R. Ferrari, 2010: Rapid changes in mixed layer stratification driven by submesoscale instabilities and winds. *Journal of Geophysical Research*, **115 (C3)**, C03 017, doi:10.1029/2008JC005203, URL http://doi.wiley.com/10.1029/2008JC005203.

Mahadevan, A., L. N. Thomas, and A. Tandon, 2008: Comment on "Eddy/Wind Interactions Stimulate Extraordinary Mid-Ocean Plankton Blooms". *Science*, **320 (448b)**, doi:10.1126/science.1152111.

Naveira Garabato, A. C., and Coauthors, 2001: Mesoscale Subduction at the Antarctic Polar Front Driven by Baroclinic Instability. *Journal of Physical Oceanography*, **31 (8)**, 2087–2107, doi:10.1175/1520-0485, URL http://journals.ametsoc.org/doi/abs/10.1175/1520-0485.

Orsi, A. H., T. Whitworth III, and W. D. Nowlin, 1995: On the meridional extent and fronts of the Antarctic Circumpolar Current. *Deep-Sea Research I*, **42 (5)**, 641–673.

Pardo, P. C., F. Pérez, S. Khatiwala, and A. Ríos, 2014: Anthropogenic CO2 estimates in the Southern Ocean: Storage partitioning in the different water masses. *Progress in Oceanography*, **120**, 230–242, doi:10.1016/j.pocean.2013.09.005.

Pujol, M.-I., Y. Faugère, G. Taburet, S. Dupuy, C. Pelloquin, M. Ablain, and N. Picot, 2016: DUACS DT2014 : the new multi-mission altimeter dataset reprocessed over 20 years. *Ocean*

533 *Science Discussions*, **0**, 1–48, doi:10.5194/os-2015-110, URL http://www.ocean-sci-discuss.
534 net/os-2015-110/.

535 Rocha, C. B., T. K. Chereskin, S. T. Gille, and D. Menemenlis, 2016: Mesoscale to Submesoscale
536 Wavenumber Spectra in Drake Passage. *Journal of Physical Oceanography*, **46 (2)**, 601–620,
537 doi:10.1175/JPO-D-15-0087.1, URL http://journals.ametsoc.org/doi/10.1175/JPO-D-15-0087.
538 1.

539 Rosso, I., A. M. Hogg, A. E. Kiss, and B. Gayen, 2015: Topographic influence on submesoscale
540 dynamics in the Southern Ocean. *Geophysical Research Letters*, **42 (4)**, 1139–1147, doi:10.
541 1002/2014GL062720, URL http://doi.wiley.com/10.1002/2014GL062720.

542 Sabine, C. L., and Coauthors, 2004: The oceanic sink for anthropogenic CO2. *Science (New York,*
543 *N.Y.)*, **305 (5682)**, 367–71, URL http://science.sciencemag.org/content/305/5682/367.abstract.

544 Sallée, J.-B., R. J. Matear, S. R. Rintoul, and A. Lenton, 2012: Localized subduction of anthro-
545 pogenic carbon dioxide in the Southern Hemisphere oceans. *Nature Geoscience*, **5 (8)**, 579–584,
546 doi:10.1038/ngeo1523, URL http://www.nature.com/doifinder/10.1038/ngeo1523.

547 Sallée, J. B., K. Speer, and R. Morrow, 2008: Response of the Antarctic Circumpolar Current to
548 Atmospheric Variability. *Journal of Climate*, **21 (12)**, 3020–3039, doi:10.1175/2007JCLI1702.
549 1, URL http://journals.ametsoc.org/doi/abs/10.1175/2007JCLI1702.1.

550 Sallée, J.-B., K. Speer, S. Rintoul, and S. Wijffels, 2010: Southern Ocean Thermocline Ventilation.
551 *Journal of Physical Oceanography*, **40 (3)**, 509–529, doi:10.1175/2009JPO4291.1, URL http:
552 //journals.ametsoc.org/doi/abs/10.1175/2009JPO4291.1.

Shakespeare, C. J., 2016: Curved Density Fronts: Cyclogeostrophic Adjustment and Frontogenesis. *Journal of Physical Oceanography*, **46 (10)**, 3193–3207, doi:10.1175/JPO-D-16-0137.1, URL http://journals.ametsoc.org/doi/10.1175/JPO-D-16-0137.1.

Sybrandy, A. L., P. P. Niiler, C. Martin, W. Scuba, E. Charpentier, and D. T. Meldrum, 2009: Global Drifter Programme: Barometer Drifter Design Reference, DBCP Report No.4, Rev 2.2. Tech. rep.

Taylor, J. R., and R. Ferrari, 2009: On the equilibration of a symmetrically unstable front via a secondary shear instability. *Journal of Fluid Mechanics*, **622**, 103, doi:10.1017/S0022112008005272.

Thomas, L. N., A. Tandon, and A. Mahadevan, 2008: Submesoscale processes and dynamics. *Ocean Modeling in an Eddying Regime*, H. Hecht, M., Hasume, Ed., American Geophysical Union, Washington, D. C., 17–38, doi:10.1029/177GM04, URL http://doi.wiley.com/10.1029/177GM04.

Thomas, L. N., and J. R. Taylor, 2010: Reduction of the usable wind-work on the general circulation by forced symmetric instability. *Geophysical Research Letters*, **37 (18)**, doi:10.1029/2010GL044680, URL http://doi.wiley.com/10.1029/2010GL044680.

Thomas, L. N., J. R. Taylor, E. A. D'Asaro, C. M. Lee, J. M. Klymak, and A. Shcherbina, 2016: Symmetric Instability, Inertial Oscillations, and Turbulence at the Gulf Stream Front. *Journal of Physical Oceanography*, **46 (1)**, 197–217, doi:10.1175/JPO-D-15-0008.1, URL http://journals.ametsoc.org/doi/10.1175/JPO-D-15-0008.1.

Thomas, L. N., J. R. Taylor, R. Ferrari, and T. M. Joyce, 2013: Symmetric instability in the Gulf Stream. *Deep Sea Research Part II: Topical Studies in Oceanography*, **91**, 96–

110, doi:10.1016/j.dsr2.2013.02.025, URL http://www.sciencedirect.com/science/article/pii/S0967064513000829.

Thompson, A. F., A. Lazar, C. Buckingham, A. C. Naveira Garabato, G. M. Damerell, and K. J. Heywood, 2016: Open-Ocean Submesoscale Motions: A Full Seasonal Cycle of Mixed Layer Instabilities from Gliders. *Journal of Physical Oceanography*, **46 (4)**, 1285–1307, doi:10.1175/JPO-D-15-0170.1, URL http://journals.ametsoc.org/doi/10.1175/JPO-D-15-0170.1.

LIST OF TABLES

589 TABLE 1. True drifter and Seasoar leg headings. The along-front direction, θ_{along}, is defined by the drifter,
590 D16, trajectory. The cross-front direction, θ_{cross}, is θ_{along} - 90. The mean true heading of Seasoar legs, θ_{leg},
591 are calculated with cross-front distance increasing away from the eddy center. Legs are projected onto a cross-
592 frontal axis through a rotation of $\theta_{rot} = \theta_{cross} - \theta_{leg}$. The axis projection alters the horizontal spacing of survey
593 measurements by the multiplication factor, $\cos(\theta_{rot})$. Legs labeled N-S correspond to section labels in Figure 5.

Leg	θ_{along}	θ_{cross}	θ_{leg}	θ_{rot}	$\cos(\theta_{rot})$
13 (N)	74.5	344.5	340.4	4.1	1.00
14	83.7	353.7	344.1	9.6	0.99
17	109.5	19.5	343.7	35.8	0.81
19	143.3	53.4	42.1	11.2	0.98
20 (NE)	157.6	67.6	52.8	14.8	0.97
21	179.2	89.3	51.2	38.1	0.79
22	200.5	110.5	101.1	9.4	0.99
23	200.5	110.5	127.2	-16.7	0.96
24	202.1	112.1	119.3	-7.1	0.99
25	206.4	116.4	131.9	-15.5	0.96
26 (E)	209.5	119.5	132.9	-13.4	0.97
27	215.7	125.7	137.7	-12.1	0.98
28	216.0	126.0	121.9	4.1	1.00
29 (SE)	214.8	124.8	119.4	5.4	1.00
32	232.1	142.1	169.6	-27.5	0.89
33	240.7	150.7	170.2	-19.4	0.94
35 (S)	284.2	194.2	179.9	14.3	0.97
36	296.8	206.8	179.4	27.4	0.89
37	296.5	206.5	179.8	26.7	0.89
38	305.8	215.8	179.4	36.3	0.81
39	309.2	219.2	180.1	39.1	0.78
40	311.5	221.5	189.8	31.7	0.85
41	26.0	296.0	325.4	-29.4	0.87
43	53.1	323.1	1.7	38.6	0.78
44	71.2	341.2	345.1	-3.9	1.00

LIST OF FIGURES

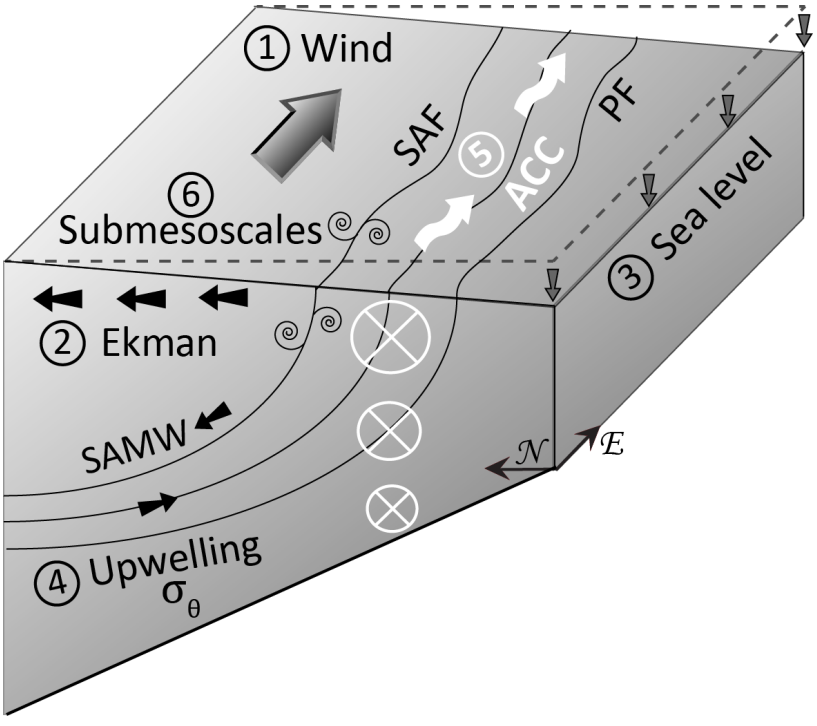

675 FIG. 1. Schematic of wind-driven upwelling in the Southern Ocean. The Antarctic Circumpolar Current
676 (ACC), Subantartic and Polar fronts (SAF, PF) and Subantarctic Mode water (SAMW) locations are labeled.

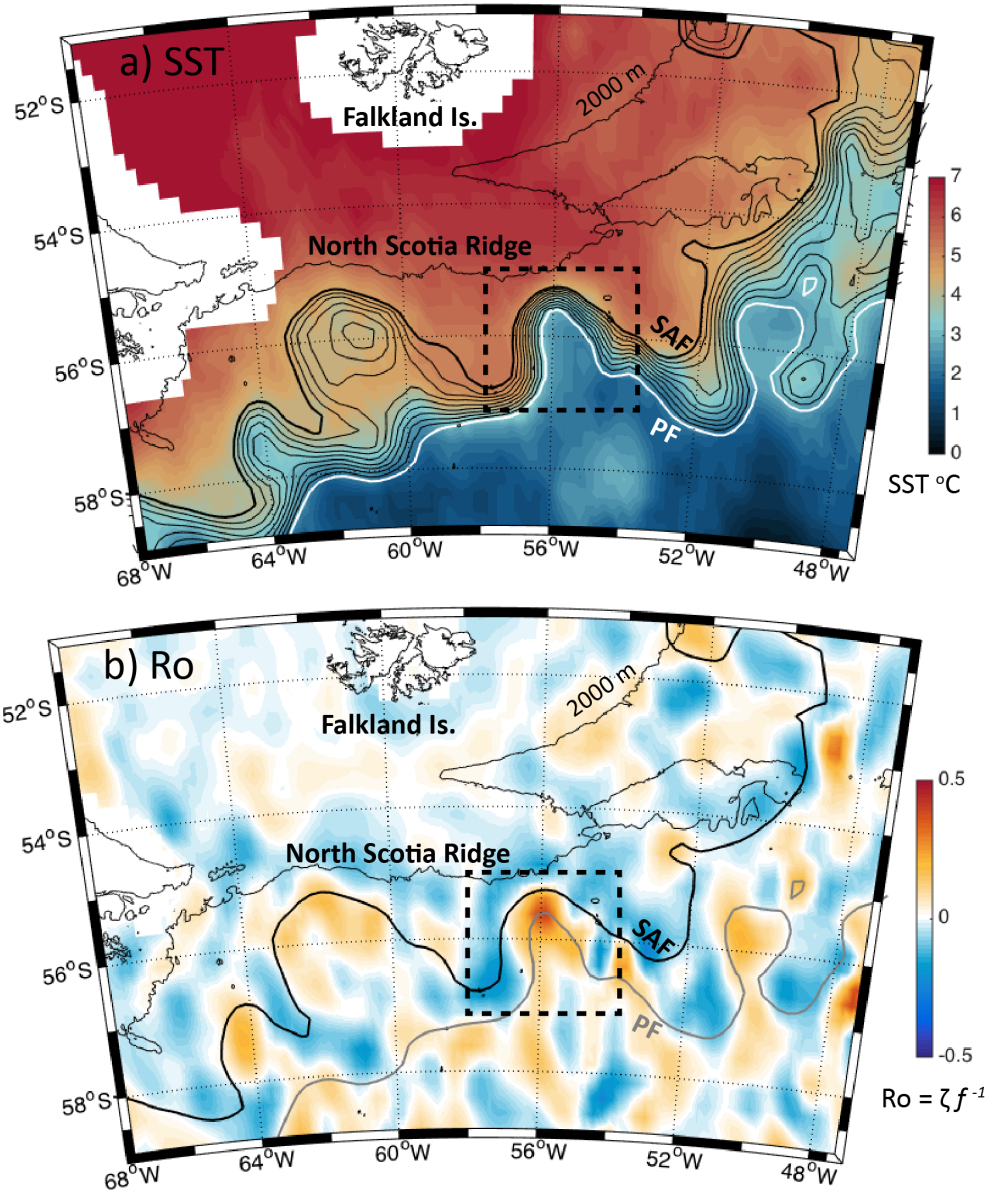

677 FIG. 2. a) A northward meander (dashed box) of the ACC in the Scotia Sea observed remotely on 20 April
678 2015 is characterized by sharp horizontal gradients of SST (°C; color) and SSH (m; contours). b) Same for
679 vorticity Rossby number (color) calculated from altimetry-derived geostrophic surface currents for 20 April
680 2015. SSH contours corresponding to the Subantarctic (SAF; -0.25 m) and Polar (PF; -0.70 m) fronts define the
681 northern and southern edges of the meander, respectively. The 2000-m isobath from GEBCO outlines the North
682 Scotia Ridge, the northern boundary of the Scotia sea.

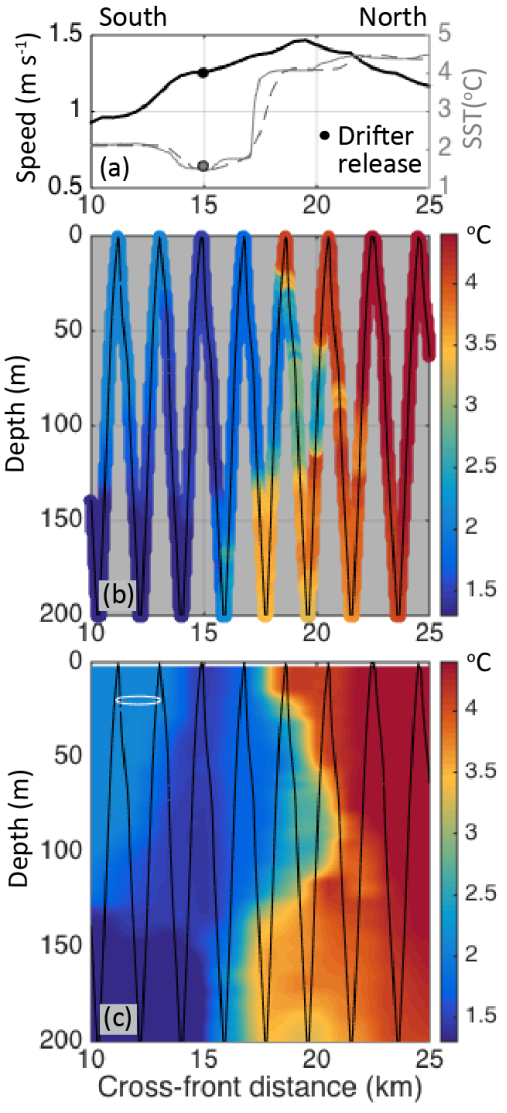

FIG. 3. a) Measured jet speed (m s^{-1}) at 50-m depth and underway SST (°C) at 4-m depth during the first Seasoar leg in survey. Gridded Seasoar temperature at 5-m depth is dashed. Drifters were released in the cold filament (1.56 °C) with jet speed $\sim$ 1.25 m s^{-1}, approximately 15 km from the start of the Seasoar leg. b) Temperature data binned into 0.5-m intervals for the first Seasoar leg. c) Same as (b) for gridded temperature data with the interpolation window, 2 km by 4 m, shown as an ellipse (white). The location of Seasoar measurements in (b) and (c) are black.

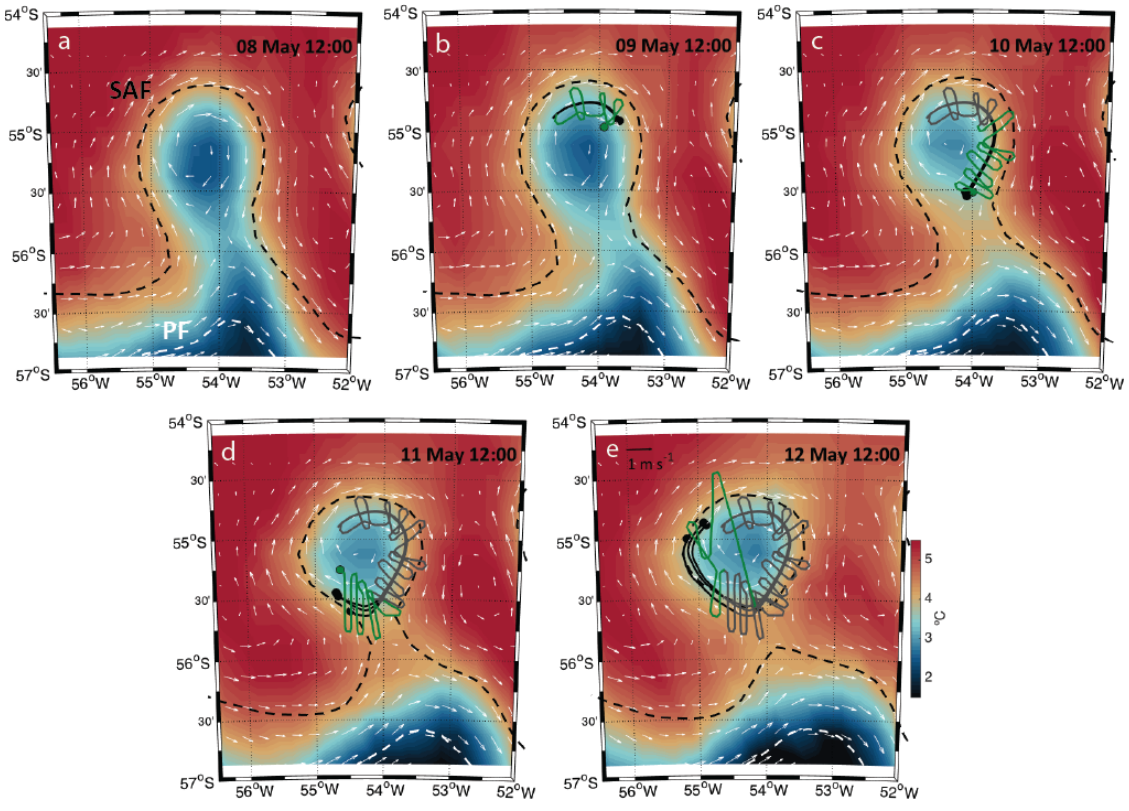

689 FIG. 4. Daily snapshots of microwave SST (REMSS) and altimetric geostrophic surface current vectors
690 (AVISO) for 8 to 12 May 2015 capturing the formation of a mesoscale eddy from a northward meander along
691 the ACC in the Scotia Sea (Figure 2). A drifter triplet shown in black was released on 08 May 20:00 GMT in the
692 northwestern sector of the meander and followed whilst towing Seasoar with the RRS JCR (green). Positions of
693 the SAF and PF, defined by the -0.25-m and -0.70-m SSH contours, are shown in black and white dashed lines,
694 respectively.

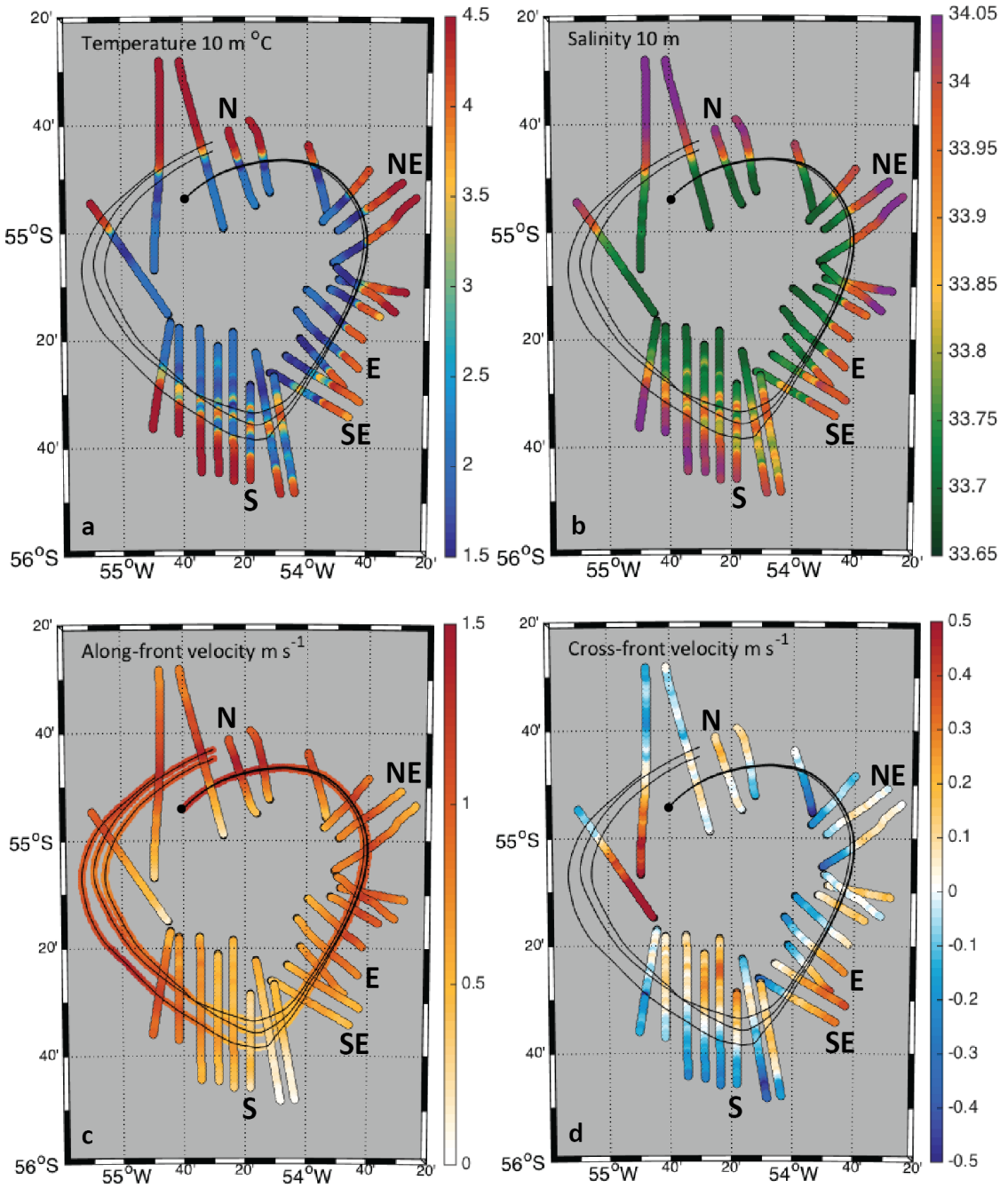

FIG. 5. Maps of 10-m depth (a) temperature and (b) salinity and 50-m depth (c) along-front and (d) cross-front velocity measurements from the drifter-following Seasoar survey introduced in Figure 4. A circle marks the starting position of the cyclonic survey. Drifter triplet tracks are shown in black except in (c) where drifter speed is also in color. Positive along-front velocities indicate a cyclonic (clockwise) direction where as positive cross-front velocities indicate flow out of the eddy. Labeled Seasoar legs, indicating the approximate location in the survey, are presented in Figure 7.

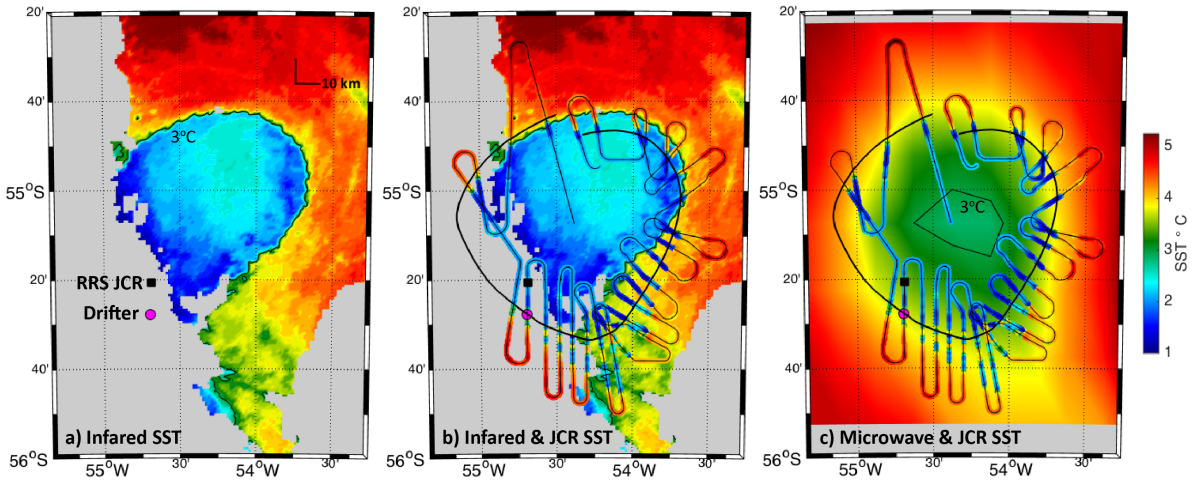

FIG. 6. (a) Level 2 infrared SST measured at 11 May 2015 12:42 GMT by an AVHRR sensor with 1-km horizontal resolution on the Metop-a satellite as the drifters (•) and the RRS JCR (■) were completing the southwest sector of the Seasoar survey. (b) JCR underway temperature data measured during the survey at 4-m depth and 40-m horizontal resolution overlaid on (a). A drifter track (black) is included. (c) Same as (b) overlaid on microwave SST (OISST; www.remss.com). The 3°C isotherm (black) outlines the eddy edge in (a) and the eddy center in (c).

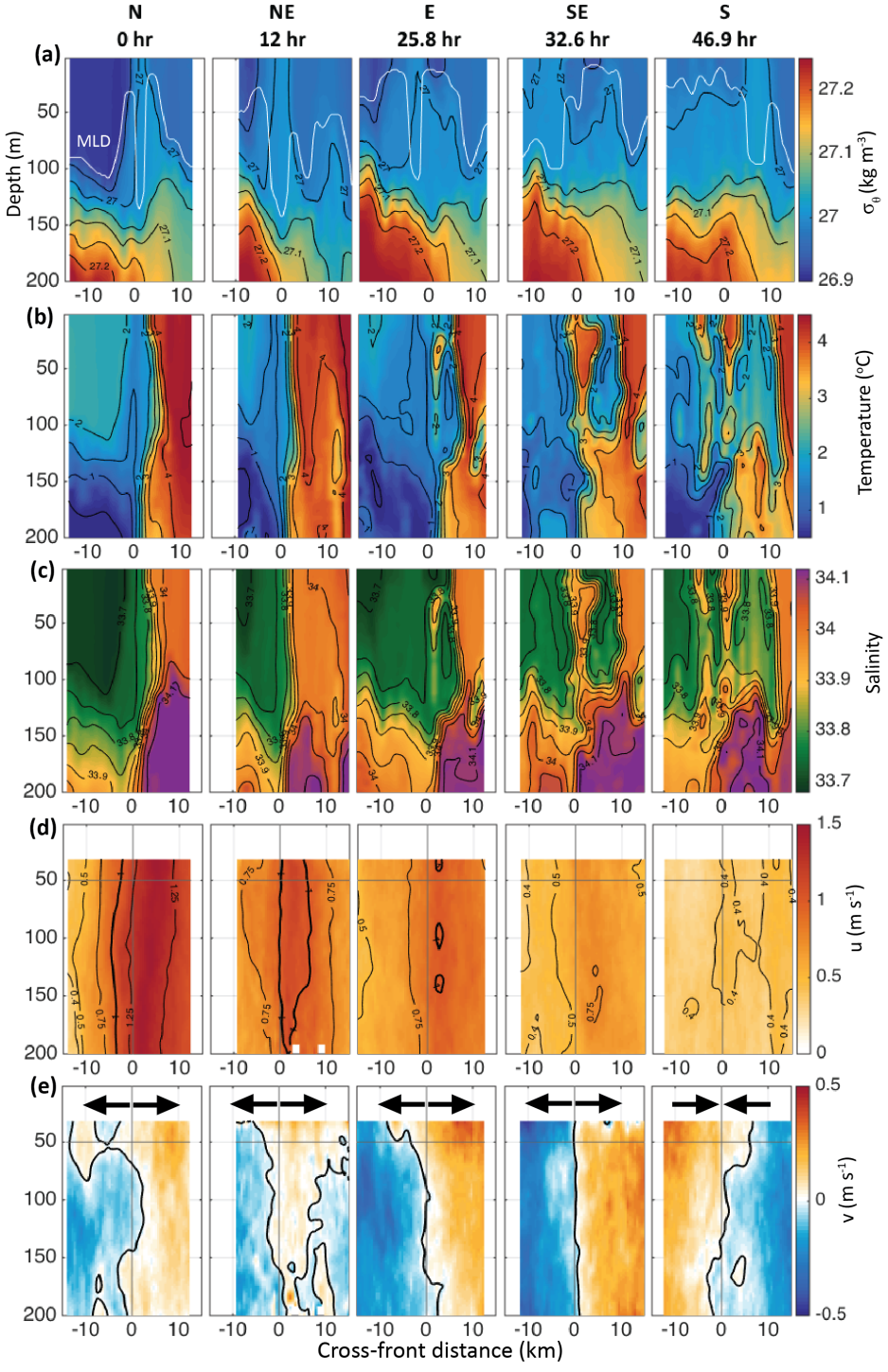

FIG. 7. Vertical cross-front sections of (a) potential density anomaly (kg m^{-3}), (b) temperature (°C), (c) salinity, (d) along-front velocity and (e) cross-front velocity for Seasoar legs N to S. The start time since the start of leg N is reported above (a) in hours. Sections are oriented such that cross-front distance increases away from the meander and eddy center. Mixed layer depth (MLD) defined as a 0.01 kg m^{-3} density difference from the surface is white in (a). The drifter location during each leg is at cross-front distance = 0 and depth = 50 m, shown at the intersection of gray lines in (c) and (d).

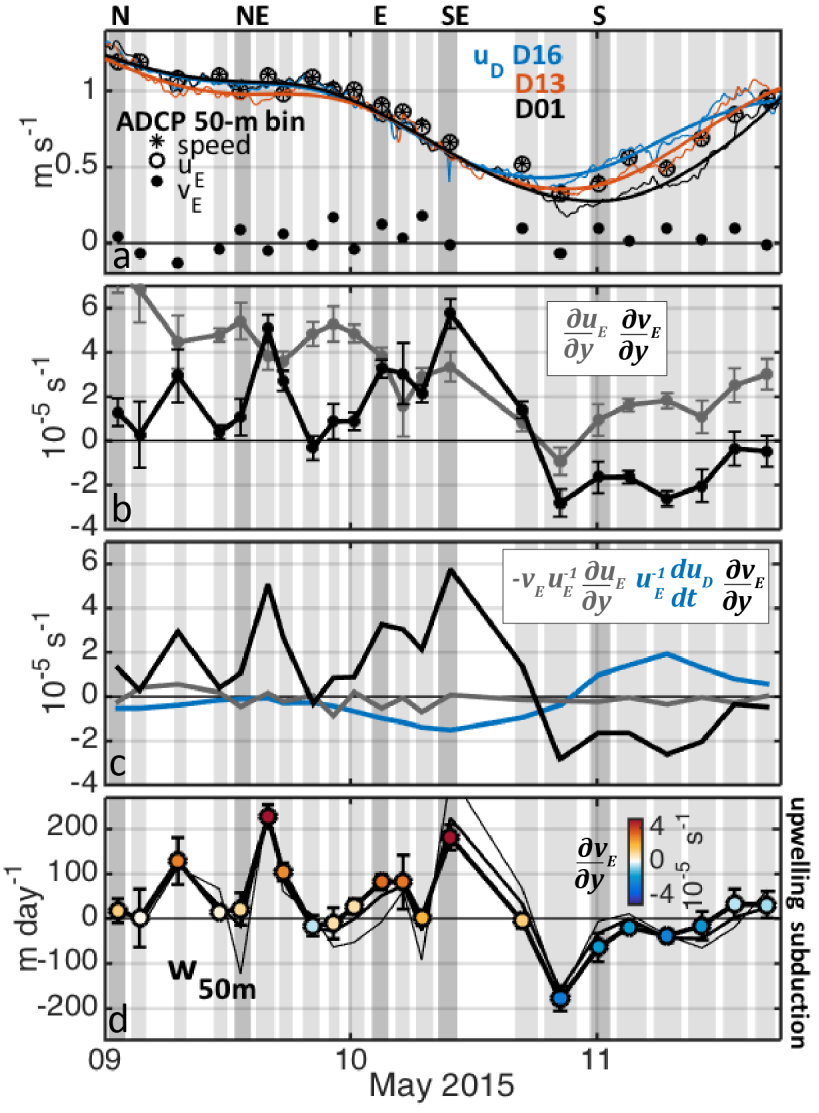

FIG. 8. (a) Time series of along-front drifter velocity, u^D (m s^{-1}), for the three drifters released and followed during the Seasoar survey from 9 to 12 May 2015. Along-front, x, and cross-front, y, water velocity components, u_E and v_E, measured within 1 km of the frontal center are shown for the drifter drogue depth of 50 m. Water speed (*) is also included. (b) Cross-front gradients of u_E (gray) and v_E (black) at 50-m depth and averaged +/- 1 km across the front. Negative $\frac{\partial \bar{v}_E}{\partial y}$ (black) indicates confluent flow. Error bars indicate uncertainty of the ADCP measurements. (c) Estimation of terms in Equation 9 after making steady-state assumption. (d) Vertical velocity at the drogue depth of 50 m, $w_{50\mathrm{m}}$ (m day^{-1}), with $\frac{\partial \bar{v}_E}{\partial y}$ (s^{-1}), from panel (b) shown in color. Error velocities of the ADCP are propagated through the calculation of w and are shown as error bars. Additional estimates of w are included for the slab (black) and linear (gray) extrapolations of u_E and v_E to the surface. Vertical velocities and $\frac{\partial \bar{v}_E}{\partial y} < 0$ indicate subduction and confluence, respectively. The duration of Seasoar legs is shaded in each panel.

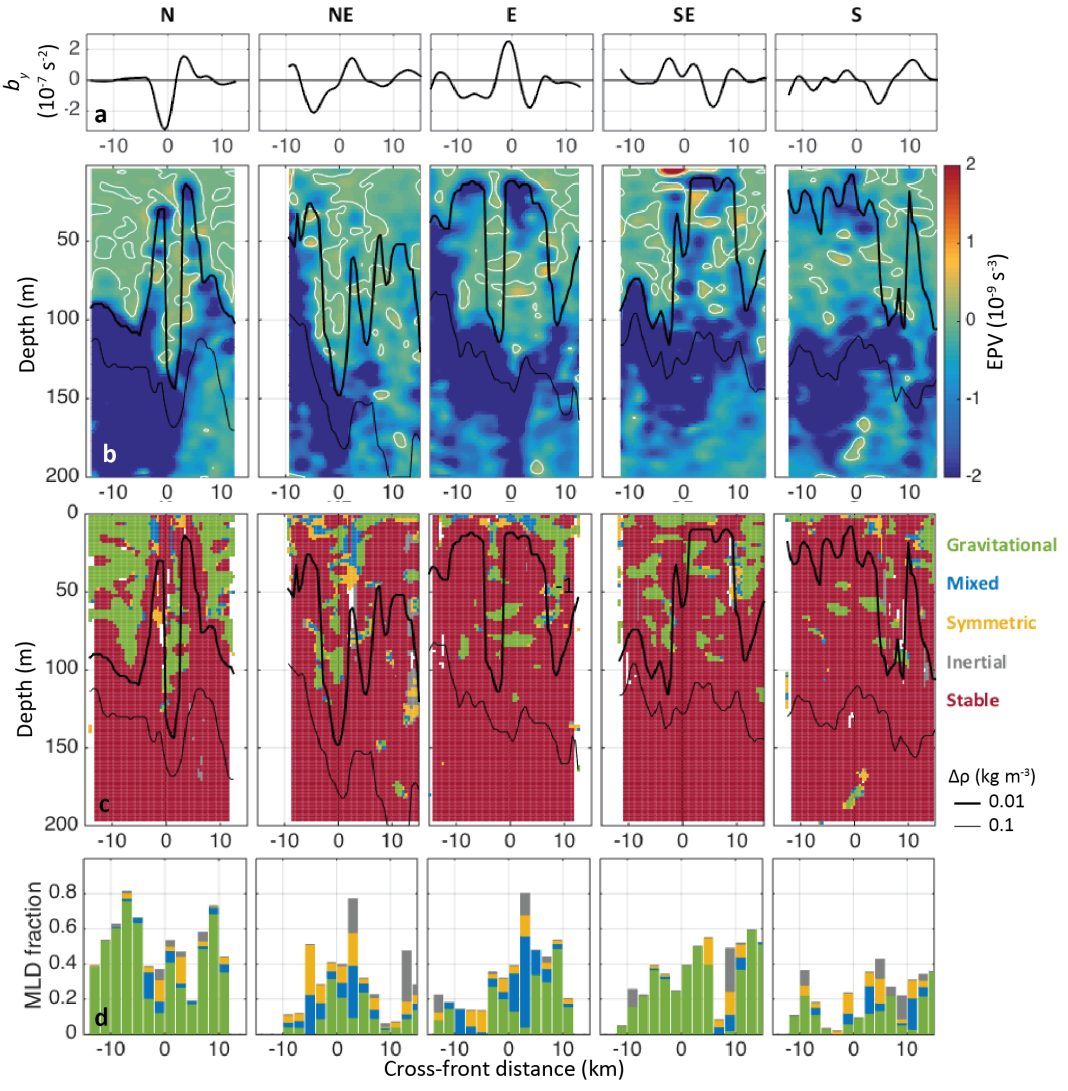

724 FIG. 9. (a) Cross-front buoyancy gradient, b_y, (s^{-2}) calculated at 10-m water depth for Seasoar legs N to
725 S. Legs are oriented with the inside of the meander and eddy on the left-hand side of each panel. (b) A 2-
726 dimensional estimate of Ertel potential vorticity (s^{-3}) is shown with the zero contour in white and the MLD,
727 defined as a 0.01 (0.1) kg m^{-3} density difference from the surface, as a thick (thin) black line. (c) Submesoscale
728 instability analysis results based on the Ri_B criteria. (d) Instances of instabilities identified in (c) shown as a
729 fraction of the 0.01 kg m^{-3} density difference MLD.

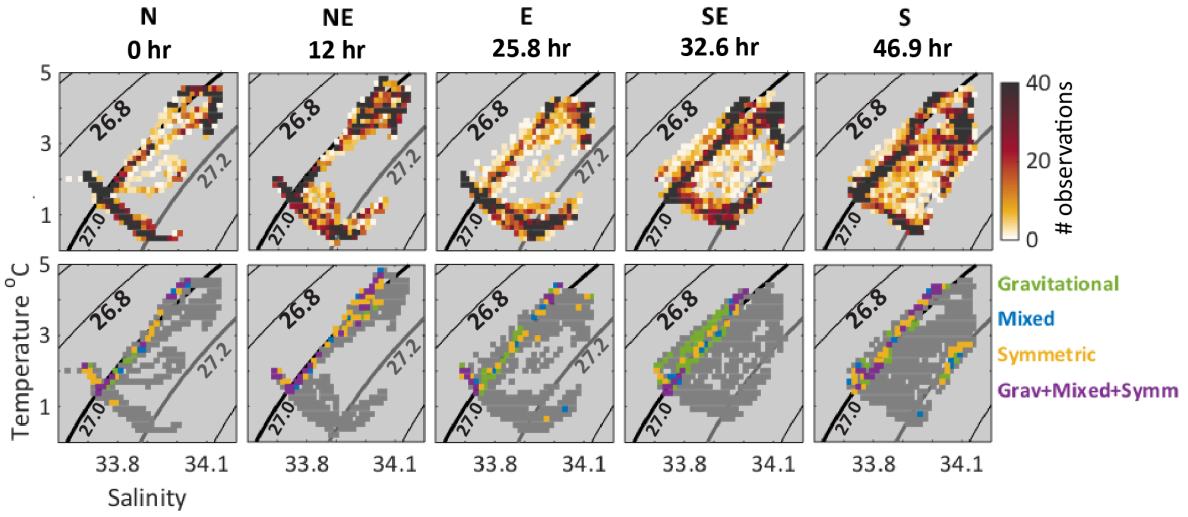

730 FIG. 10. T-S diagram histograms for Seasoar legs N to S. (a) Color indicates number of measurements in
731 0.15°C and 0.015 salinity bins and (b) instability types in the mixed layer as diagnosed in Section 3d. The cold,
732 fresh observations inside the meander and eddy occupy the bottom left 'hot spot' of measurements in T-S space
733 in Leg N. An exchange along isopycnals $\sigma_{\theta 27}$ (bold) and $\sigma_{\theta 27.2}$ (gray) occurs over this series.

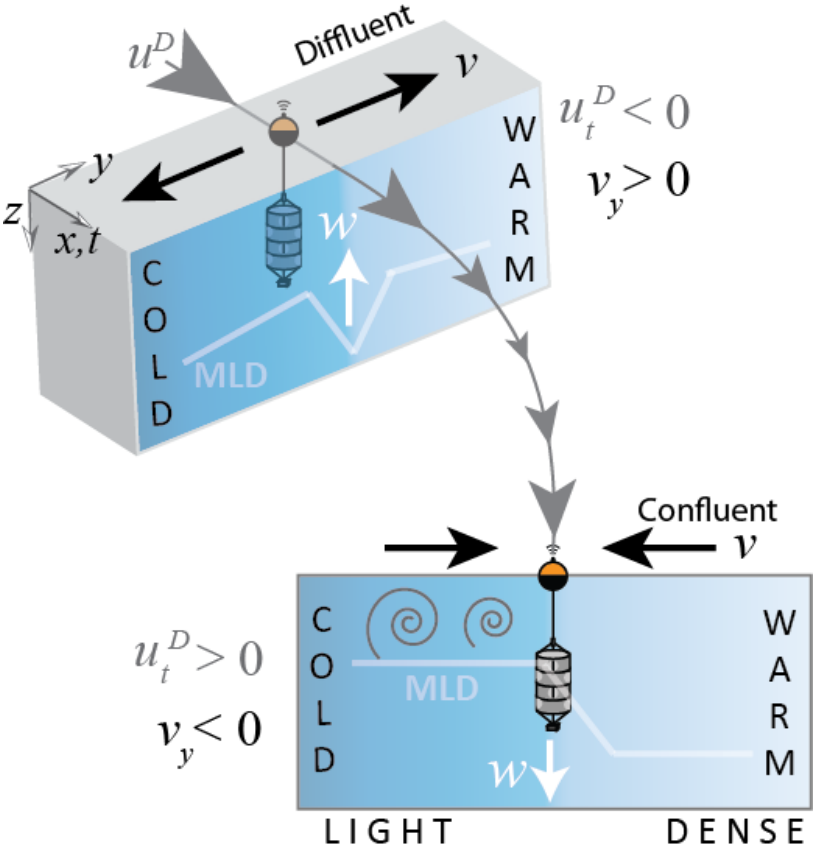

734 FIG. 11. Cartoon summarizing frontal circulation during eddy formation. The two cross-frontal sections
735 represent the northern and southern sectors of the survey, legs N and S.

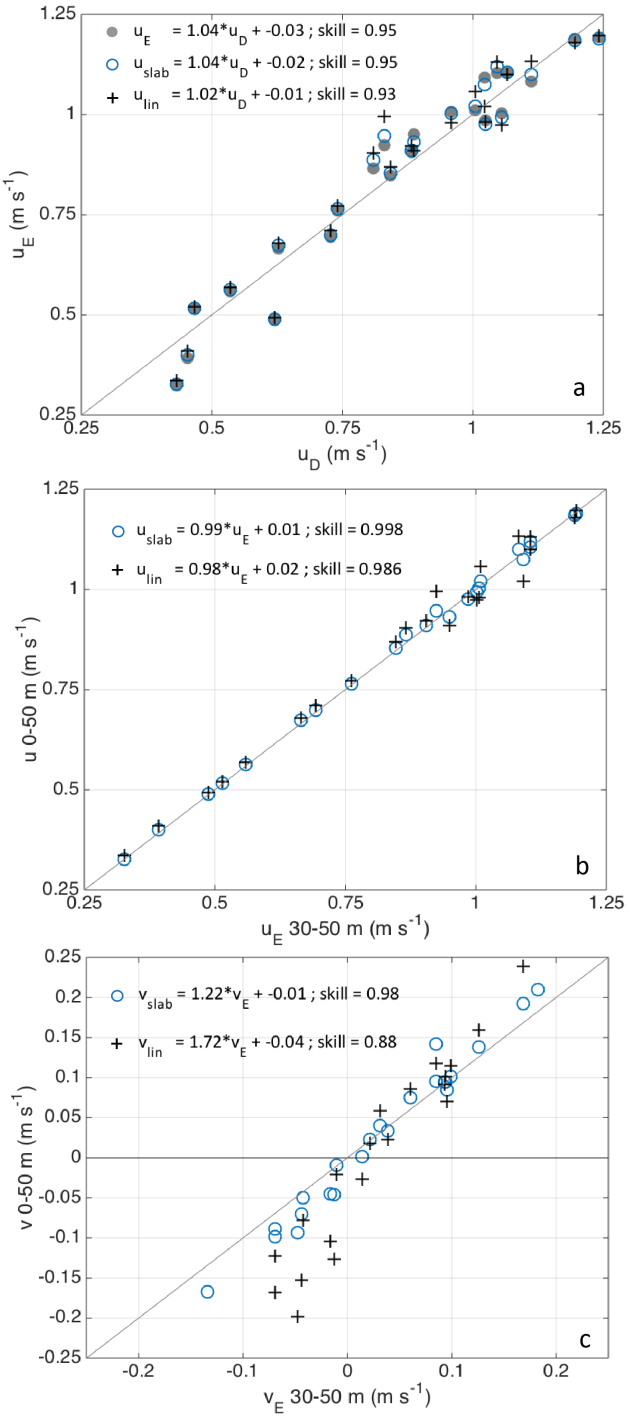

FIG. A1. (a) Drogued drifter velocities (u_D) compared with depth-averaged Eulerian velocities between 30 and 50 m (u_E, •) and approximations of u_E from 0 to 50 m using slab (○) and linear (+) extrapolations. (b) Comparison of the measured u_E (30 to 50 m) to the extrapolated approximations (0 to 50 m). (c) Same as (b) for v_E. Linear regression fits and respective skills, var(fit) / var(data), are reported in each panel.

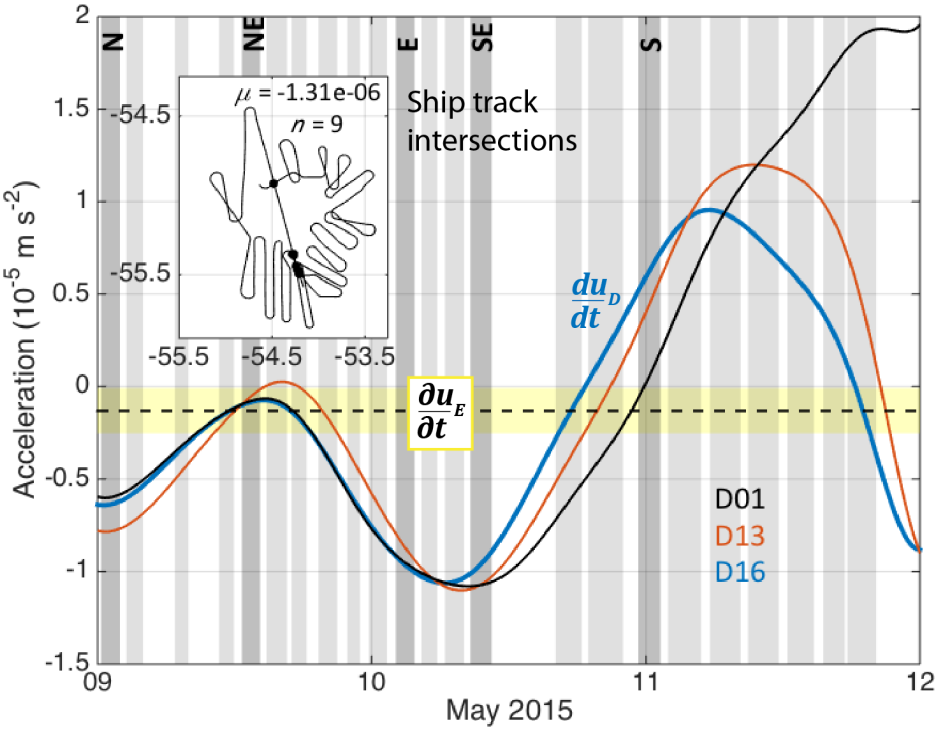

740 FIG. A2. Estimates of Eulerian local acceleration during the Seasoar survey calculated from ship track inter-
741 sections (map inset) during the Seasoar survey. Gray bars show the duration of each Seasoar leg; the N-S legs
742 (dark gray) are labeled.